Proceedings of the Thirty-sixth (2026) International Ocean and Polar Engineering Conference **www.isope.org**
Orlando, Florida, USA, May 31-June 5, 2026

ISBN 978-1-880653-72-2; ISSN 1098-6189

Numerical Simulation of Flow Field Interference among Multiple Substructures of a Floating Offshore Wind Platform

*Qinwen Zhang, Jianhua Wang, Decheng Wan**

Computational Marine Hydrodynamics Laboratory (CMHL), School of Ocean and Civil Engineering,
Shanghai Jiao Tong University, Shanghai, China
*Corresponding author

ABSTRACT

As global energy development extends into deep and ultra-deep waters, offshore platforms have been widely employed in oil and gas exploitation as well as offshore wind power generation. The underwater structures of these platforms are typically composed of multiple structural components, including piles, columns, pontoons (ballast tanks), truss structures, mooring systems, and frame assemblies. In complex marine environments, the flow fields around these structures exhibit strong coupling effects, leading to intricate hydrodynamic interactions. Such interference not only alters the local fluid dynamic characteristics but also affects the load distribution and vortex shedding patterns acting on the platform. Consequently, these phenomena have significant impacts on the structural safety, stability, and service life of offshore platforms.To investigate the characteristics of the surrounding flow field of offshore platforms under three-dimensional flow conditions, this study conducts numerical simulations on a representative floating offshore wind power platform. The simulations are based on the incompressible Navier–Stokes equations, employing the SST-DES turbulence model within the computational fluid dynamics (CFD) software STAR-CCM+. The obtained results include the velocity field distribution and wake vortex evolution around the platform. The findings aim to provide theoretical support and technical reference for structural design, layout optimization, and hydrodynamic performance improvement of offshore platforms.

KEY WORDS: Marine platform; Underwater structure; Flow field interference; Numerical simulation

INTRODUCTION

As resource development gradually moves towards the deep-sea area, energy development carriers centered around marine platforms have developed rapidly. At the same time, their structural safety and stability are facing severe challenges. The underwater multi-column support system, due to its strong carrying capacity and stability, is widely used in various marine platforms. The flow interference between columns may lead to flow separation, transition of gap flow state, formation of shear layers, reattachment, vortex impact, recirculation, quasi-periodic vortices and vortex bands, and their interactions. In actual sea conditions, the platform column structure often faces the coupling effect of complex flow fields such as ocean currents, waves and tides, resulting in significant flow interference effects between columns, causing complex flow phenomena such as vortex shedding, tail flow deflection, pressure superposition, local velocity enhancement, etc., which leads to distorted force distribution of the structure, intensified vibration response, and even induces structural fatigue damage, vibration instability and catastrophic failure risks. Therefore, in-depth exploration and revelation of the flow interference mechanism between underwater multi-column structures, and more accurate quantification and prediction of their hydrodynamic characteristics, have important engineering value and theoretical significance for the optimization design and safety assessment of marine platforms.

Over the years, scholars at home and abroad have conducted corresponding research and analysis on various flow-around problems using model tests and numerical simulations. From single circular columns to double circular columns and then to multi-circular columns, the research system has gradually been improved. At the same time, with the rise of numerical simulation and the maturity and popularization of CFD methods, the accuracy and reliability of the results have also been enhanced.

In the field of flow around single circular cylinder structures, for instance, large eddy simulation (LES) combined with vortex identification techniques has been employed to numerically investigate the three-dimensional flow around finite-length cylinders. The results indicate that the recirculation region behind finite-length cylinders is relatively short, and the downwash effect induced by the free end disrupts the Kármán vortex street, leading to a reduction in the drag coefficient. Compared with fixed-wall boundary conditions, the free end is more strongly influenced by the streamwise velocity. Paired “mushroom-shaped” vortices are observed on the free-end surface, accompanied by two flow source points. The flow field around finite-length cylinders exhibits more pronounced three-dimensional characteristics, resulting in smaller drag coefficients. In addition, tip vortices are formed downstream of the free end, while “horseshoe” vortices develop at the junction between the cylinder and the fixed wall(Wang et al., 2018). Relevant researchers conducted numerical simulations of three-dimensional flow past a circular cylinder at a subcritical Reynolds number of Re=3900 using the unsteady Reynolds-averaged Navier–Stokes (URANS) approach and the detached-eddy simulation (DES) method, respectively. The numerical results obtained from both approaches were compared with available experimental data. The study demonstrated that, compared with the

URANS method, the DES approach is capable of capturing more detailed and accurate flow-field characteristics in the vicinity of the cylinder (Zhao et al., 2016). Subsequently, researchers employed the delayed detached-eddy simulation (DDES) technique in combination with the piecewise linear interface calculation (PLIC) method to numerically investigate the flow around finite-length cylinders with a free surface. The simulation results indicated that both the free surface and the free end exert distinct influences on the flow characteristics around the cylinder, significantly altering the distribution of the flow field along the draft direction(Chen et al., 2022).
In the field of flow around dual circular cylinders, previous studies have systematically summarized the interference characteristics under tandem and side-by-side arrangements. A wake interference classification scheme based on the inter-cylinder spacing was proposed, and the typical features of vortex shedding structures in different interference regimes were elucidated（Zdravkovich., 1987). In addition, model experiments were conducted to investigate the flow characteristics of two tandem square cylinders at Reynolds numbers ranging from $2.0\times10^3$to 1.6×10^4under different inter-cylinder spacing conditions. The results revealed that the flow-field features of tandem cylinders are not only dependent on the spacing between the cylinders but are also influenced by the tandem arrangement. Moreover, the vortex shedding hysteresis phenomena induced by increasing and decreasing inter-cylinder spacing exhibit distinct behaviors(Liu and Chen, 2002). Subsequent researchers employed large eddy simulation (LES) to investigate the flow characteristics of tandem dual circular cylinders. The results indicated that when the spacing ratio is smaller than a critical value, vortex shedding occurs only from the downstream cylinder(Kitagawa and Ohtab, 2008).
In the field of flow around multiple cylinders, researchers have employed the lattice Boltzmann method to investigate the flow interference characteristics of four circular cylinders arranged in a diamond configuration. The results indicate that the flow patterns around the four cylinders vary under different spacing ratios, and that there exists an optimal spacing ratio at which the drag coefficients of the individual cylinders attain their minimum values(Gong et al., 2015). Subsequent studies demonstrated that, under incoming flow angles of 0° and 45°, the vortex shedding frequencies of individual columns within an array of four vertical piles are higher than those of a single isolated column, and that the vortex shedding pattern exhibits a typical 2S mode(Liu et al., 2015).
This paper focuses on the flow disturbance problem of the underwater multi-column structure of the marine platform. For the OC4 floating wind turbine platform model, a three-dimensional flow numerical model was constructed using the CFD software STAR-CCM+, based on the SST-DES model to capture the complex tail flow evolution behavior. By comparing the drag coefficients, velocity distributions, and tail vortex shedding conditions at different column positions. The coupling mechanism of column size, free end of the column, and inter-column interference was systematically discussed. The research results can provide theoretical basis and numerical reference for the hydrodynamic design of multi-column structures, the optimization of platform anti-turbulent response, and the vibration prevention of engineering structures.

METHODOLOGY

Governing Equations

For incompressible two-phase flows, the governing equations consist of the mass conservation and momentum conservation equations, which are expressed as follows:

$$\nabla \cdot \boldsymbol{U} = 0 \tag{1}$$

$$\frac{\partial \rho \boldsymbol{U}}{\partial t} + \nabla \cdot (\rho \boldsymbol{U}\boldsymbol{U}) = -\nabla p_{\mathrm{d}} - \boldsymbol{g} \cdot \boldsymbol{x} \nabla \rho + \nabla \cdot (\mu_{\mathrm{eff}} \nabla \boldsymbol{U}) + f_{\sigma} \tag{2}$$

Here, $\boldsymbol{U}$ denotes the velocity vector; ρ represents the weighted density; p_{d} denotes the dynamic pressure; $\boldsymbol{g}$ is the gravitational acceleration vector; $\boldsymbol{x}$ is the position vector; μ_{eff} denotes the effective dynamic viscosity; f_{σ} represents the surface tension term; and t denotes time.

Turbulence Model and Detached Eddy Simulation

When high-Reynolds-number flows pass around cylindrical structures, complex shear-layer structures develop in the wake region, accompanied by periodically shed vortex streets. Such flows exhibit pronounced three-dimensional characteristics, together with evident flow separation and wake-flow instabilities. To accurately characterize the aforementioned flow structures and their evolutionary behaviors, a hybrid turbulence model coupling the shear stress transport (SST) model with detached-eddy simulation (DES) is adopted in this study. This model ensures reliable near-wall flow predictions while significantly enhancing the capability to resolve wake vortex structures.
The SST model can effectively balance the requirements of turbulence modeling in both the near-wall layer and free shear layer. It adopts the conventional model formulation in the near-wall region to ensure boundary layer resolution accuracy, and switches to the model form in the free shear region away from the wall, which not only enhances numerical stability but also avoids excessive diffusion issues. The transport equations for turbulent kinetic energy and specific turbulent dissipation rate are as follows:

$$\frac{\partial k}{\partial t} + \frac{\partial (u_j k)}{\partial x_j} = \tilde{G} - \beta^* k\omega + \frac{\partial}{\partial x_j}\left[(\nu + \alpha_k \nu_t) \frac{\partial k}{\partial x_j} \right] \tag{3}$$

$$\frac{\partial \omega}{\partial t} + \frac{\partial (u_j \omega)}{\partial x_j} = \gamma S^2 - \beta \omega^2 + \frac{\partial}{\partial x_j}[(\nu + \alpha_\omega \nu_t)\frac{\partial \omega}{\partial x_j}] + (1 - F_1) CD_{k\omega} \tag{4}$$

where $\tilde{G}$ denotes:

$$\tilde{G} = \min(G, c_1 \beta^* k\omega) \tag{5}$$

$$G = \nu_t S^2 \tag{6}$$

$CD_{k\omega}^* = \max(CD_{k\omega}, 10^{-10})$, $CD_{k\omega} = 2\alpha_{w2} \cdot \frac{1}{\omega}\frac{\partial k}{\partial x_j}\frac{\partial \omega}{\partial x_j}$, F_1 denotes the blending function.This model possesses the advantage of not relying on wall functions and being capable of directly resolving the viscous sublayer; therefore, it is well suited for high-accuracy simulations in the vicinity of structural surfaces.
Although the SST model yields excellent prediction accuracy in the near-wall region, it fails to effectively characterize the numerous unsteady, large-scale vortex shedding and evolutionary features in the wake region, and a single RANS method can hardly meet the analytical requirements. Therefore, the DES method is introduced in this study to construct a hybrid RANS/LES numerical strategy (Spalart et al., 1997). Its core lies in the following: the RANS model is retained within the boundary layer to maintain computational efficiency, while the LES mode is activated in the free shear layer; in regions where the grid resolution meets the LES solution requirements, the turbulence model degrades to a subgrid-scale model, and the Reynolds-averaged model is adopted otherwise. This strategy enables the direct resolution of vortex structures in the wake region.
In the SST-DES model, the turbulent length scale is modified in the following form:

$$l_{DES} = \min\left(\frac{k^{1/2}}{\beta^{*}\omega}, C_{DES}\cdot\Delta\right) \tag{7}$$

Herein, $\Delta = \max(\Delta x, \Delta y, \Delta z)$ denotes the local grid scale and C_{DES} is an empirical constant with a typical value of 0.61. This modification ensures that the RANS framework is maintained in the near-wall region, while a gradual transition to the LES mode is achieved in the shear flow regions far from the wall, which can effectively avoid the issues such as model delay and grid-induced separation caused by an early model switch.

As a turbulence solution model that balances efficiency and accuracy, the SST-DES model demonstrates significant application value in this study. Affected by the coupling interference between columns and the periodic shedding of vortices, the wake flow field exhibits strong three-dimensional and transient flow characteristics. The SST-DES model can overcome the limitations of traditional RANS methods, clearly analyze the evolution of the shear layer at the column tail and the generation and shedding mechanism of vortices between columns, and achieve precise prediction of unsteady resistance characteristics. Moreover, in the surface fluctuations and interface vortex structures induced by the column flow perturbations, this model can also effectively capture and accurately depict them, demonstrating excellent cross-scale flow adaptability.

COMPUTATIONAL MODEL AND MESH GENERATION SETUP

Computational Model

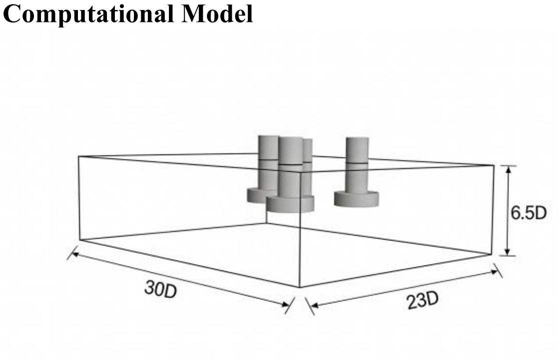

Figure. 1 Computational domain

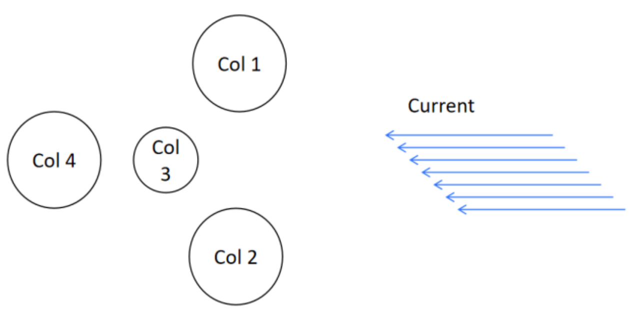

Figure. 2 Schematic of platform column layout

The size of the computational domain adopted in this study is 30D× 23D× 6.5D, as illustrated in Figure 1. The diameter D of the central cylinder Col 3 is 0.25 m, the corresponding Reynolds number Re=3.38×10^5, Froude number Fr=0.98 while the outer diameter D$_2$ and inner diameter D$_3$ of the outer cylinders are 0.93 m and 0.465 m, Re_2= 1.26×10^6, Fr_2=0.51; Re_3=6.28×10^5, Fr_3=0.72. respectively. The spacing between the outer cylinders and the central cylinder is 1.12 m, and the submerged depth of the cylinders is 0.775 m. The incoming flow velocity is set to 1.54 m/s. The density and kinematic viscosity of water are taken as 1000 kg/m^3 and 1.14×10^{-6} m^2/s, respectively; the corresponding values for air are 1 kg/m^3 and 1.48×10^{-5} m^2/s. The time step is set to 0.002 s, ensuring that the Courant number remains below 1 at all times. A total of 8 boundary layer grids are arranged on the cylindrical surface, with the height of the first wall-adjacent cell satisfying y+ < 1. The layout of the platform columns is presented in Figure 2.

Mesh Generation Details

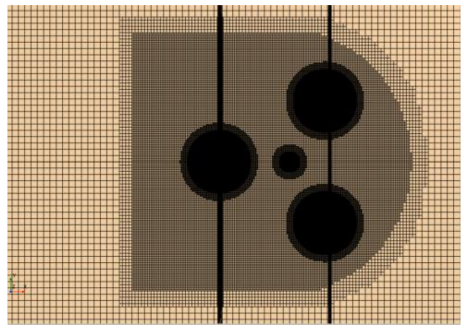

(a)

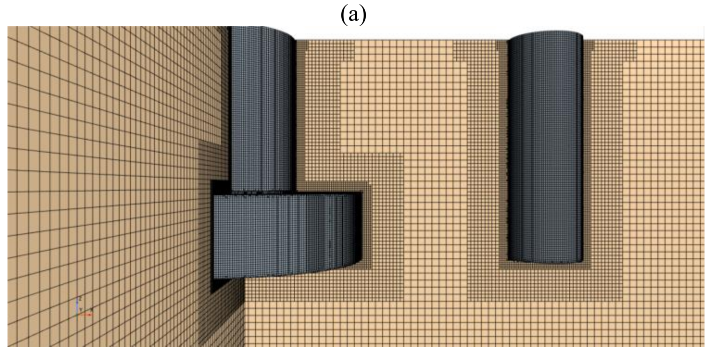

(b)

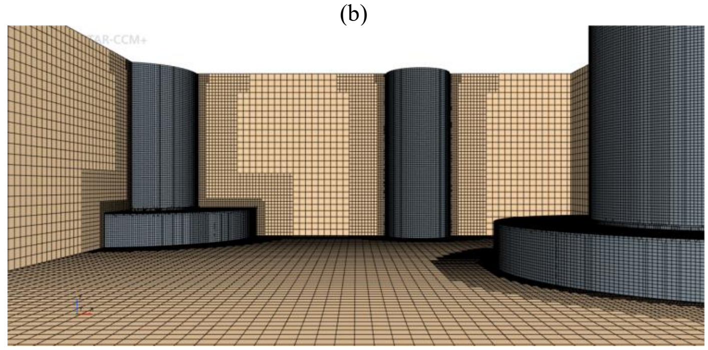

(c)

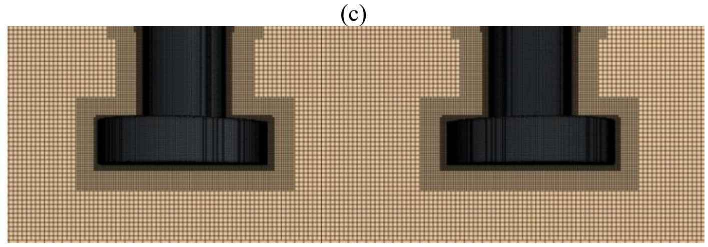

(d)

Figure. 3 Computational mesh generation: (a) Mesh generation in the x-y plane; (b) Mesh generation in the x-z plane; (c) Overall view of mesh generation in the x-z plane; (d) Mesh generation on the cylinder surface

Figure 3 illustrates the computational grid division adopted in this study. The total number of grids is 547,0000. Specifically, Figure 3(a) presents

the overall grid layout along the x-y plane. To capture the changes in the flow field more precisely, the Kelvin wave disturbance area was densified during the grid division process. Figure 3(b) shows the local densification on the x-z plane. Figure 3(c) presents the overall grid division on the x-z plane. Figure 3(d) shows the local densification around the cylindrical body on the y-z plane. Additionally, to better investigate the interference between the cylinders and the influence of the free end on the flow, local densification was performed in the corresponding focused areas to ensure the calculation accuracy.
In terms of the boundary condition setup for the computational domain, a uniform inflow velocity inlet boundary condition is applied at the upstream inlet, and a pressure outlet boundary condition is adopted at the downstream outlet. The cylinder surfaces are specified as the no-slip wall boundary condition to accurately simulate the shear effect of the wall. A symmetry boundary condition is set at the bottom of the domain, while the zero-gradient boundary condition is imposed on both the lateral and top boundaries, which allows the natural diffusion of the fluid without introducing additional disturbances.

RESULTS AND DISCUSSION

Drag Coefficient

The drag coefficient is a dimensionless parameter used to quantify the drag force acting on a body in a fluid, which is defined as follows:

$$C_D = \frac{F_x}{\frac{1}{2}\rho U^2 DH} \tag{8}$$

where: F_x is the drag force, D is the cylinder diameter, U is the incoming flow velocity, and ρ is the fluid density. H represents the immersion depth.

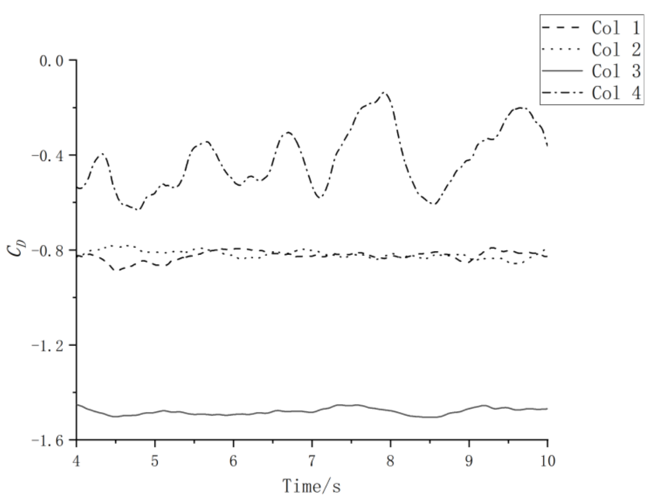

Figure. 4 Drag coefficient curves

As can be seen from Figure 4, the drag coefficients of the two upstream cylinders Col 1 and Col 2 are basically stable at approximately -0.8 with a small fluctuation amplitude, indicating that they are in a relatively stable flow around state. The drag coefficient of the middle cylinder Col 3 remains at -1.5 with negligible fluctuations and almost no obvious periodic oscillation. This phenomenon can be attributed to the fact that Col 3 is located at the confluence of the wake regions of Col 1 and Col 2 and is subject to a strong wake shielding effect. The low-velocity recirculation zone generated by the upstream cylinders significantly reduces the local velocity on the windward side of the middle cylinder, thereby decreasing the dynamic pressure contribution; Meanwhile, the disturbance of the shear layer is suppressed, and the frequency of vortex shedding decreases, resulting in a tendency for the resistance to become constant. In contrast, the drag coefficient of the downstream column Col 4 shows intense unsteady fluctuations and obvious periodic oscillation characteristics. This phenomenon indicates that the rear column is in a relatively unstable wake environment, and its flow is strongly influenced by the wakes of the middle column and the upstream columns. When the upstream vortex propagates to the rear column, it will cause alternating positive and negative pressure pulsations on its surface, thereby leading to corresponding fluctuations in the force it experiences.

Velocity Distribution

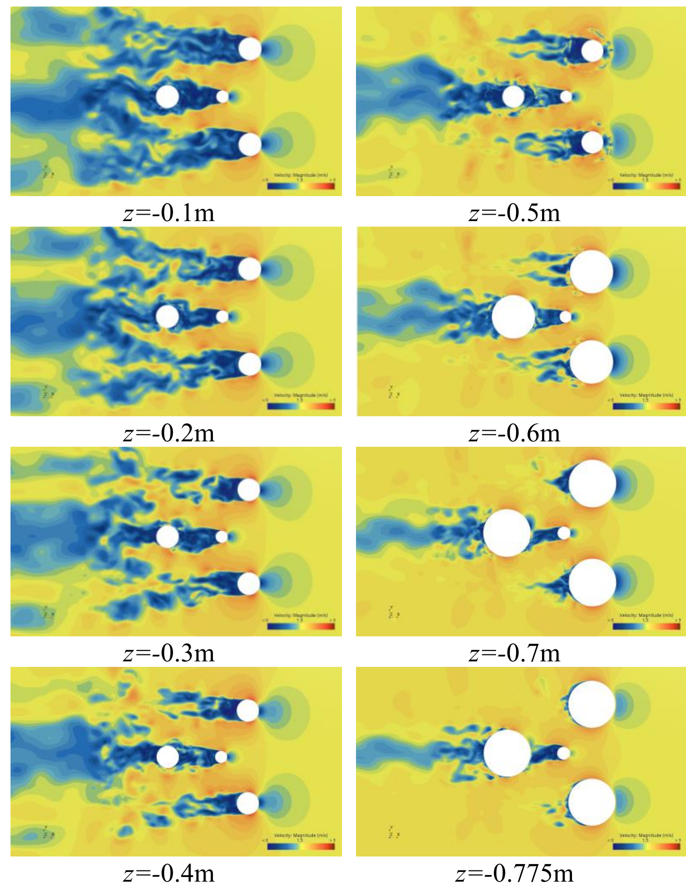

Figure. 5 Velocity magnitude distribution at different depths

In the near-free-surface region, the velocity field distribution is characterized by the horizontal expansion of the low-velocity deficit zone under compression, and the vortex street structure exhibits features of asymmetric distortion and fragmentation. The coherent superposition of the wakes from adjacent cylinders further amplifies local disturbances, resulting in weak flow field symmetry and spatial coherence. As the depth increases, the flow field gradually breaks away from the influence of the free surface, and the viscous force and inertial force reach a dynamic equilibrium. The thickness of the low-speed loss zone is uniform, and a clear Karman vortex street structure is presented along the flow direction. The adjacent cylinder wake flows into a stable phase-lock state, forming alternating distributions of low-speed vortices and velocity enhancement bands. In the vicinity of the interface region, the

flow field still maintains a quasi-steady state, with only the precursory disturbances of the near-bottom surface interference appearing.
In the near-bottom region, the viscous retardation effect of the bottom surface gradually dominates the flow field evolution. The upward transmission of viscous forces disrupts the dynamic equilibrium in the middle layer, causing the thickness of the low-velocity deficit zone to contract gradually and deflect toward the single wall-adjacent side, and the vortex street structure to break down progressively until complete disintegration. Meanwhile, the geometric scale of the large cylinders couples with the bottom retardation effect, which further exacerbates the asymmetric deformation and disturbance of the wake flow. At the transition section in the interface region, the flow field begins to exhibit asymmetric distortion; the vortex street structure is completely disrupted at a draft depth of 0.6 m; at the bottom section of the free end, the thickness of the low-velocity deficit zone reaches the minimum value across the entire depth, the flow field loses its symmetry and spatial coherence entirely, with only scattered low-velocity vortex clusters and irregular velocity enhancement bands remaining.

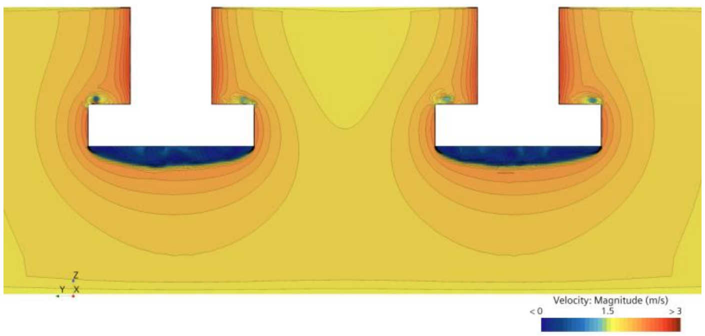

Figure. 6 Velocity magnitude distribution on the y-z cross-section of the two upstream cylinders

Figure 6 presents the velocity distribution on the y-z cross-section of the two upstream cylinders Col 1 and Col 2. In terms of the overall distribution, a prominent low-velocity region is observed in the area beneath the cylinders and near the interface zone, while local high-velocity bands and strong shear layer structures are formed in the sidewall and corner regions. This indicates that the cylindrical structure exerts a significant blockage effect on the incoming flow, leading to the redistribution of the mainstream momentum within the cross-section and the induction of complex three-dimensional flow-around structures. At the sharp corner positions on both sides of the interface zone, symmetrically distributed local low-velocity regions and vortex core structures can be identified. These regions are not directly generated by the deceleration of the incoming flow, but may mainly result from the combined effects of premature boundary layer separation caused by adverse pressure gradients induced by geometric abrupt changes, and the transport of horseshoe vortices along the sidewalls from the windward side with their retention in the corner regions. Meanwhile, the secondary flow induced under shallow water conditions causes the continuous convergence of low-momentum fluid toward these regions, which further enhances the low-velocity retention effect. A distinct high- to low-velocity shear layer is formed in the peripheral area of the low-velocity regions at the sharp corners, which may be primarily generated by the interaction between the mainstream diffraction acceleration and the recirculation zone, accompanied by local vortex activities.

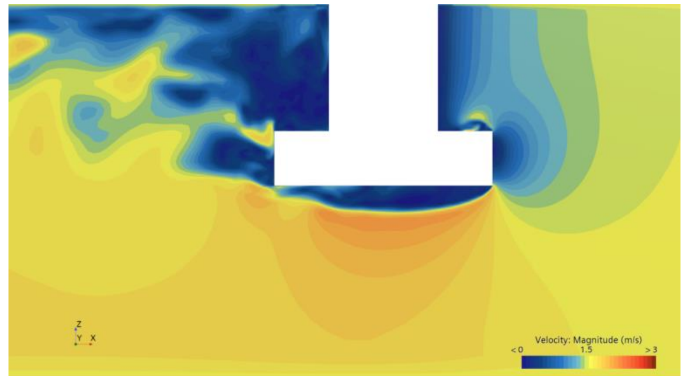

Figure. 7 Velocity magnitude distribution on the x-z cross-section of the upstream cylinders

Figure 7 shows the velocity distribution on the x-z cross-section of the upstream cylinders Col 1 and Col 2. In the vicinity of the interface position, a distinct concentrated zone of velocity gradient and local vortex structures can be observed. Owing to the significant geometric abrupt change in this region, thus generating separation bubbles and recirculation structures at the root of the corner. In addition, the upstream wall-attached flow deflects sharply at the interface and interacts with the separated flow, inducing the formation of local vortices and leading to a patchy low-velocity distribution characteristic in this region. A prominent velocity enhancement zone also appears in the free-end region due to velocity escape, and an obvious upward surging tendency is observed in the wake region near the free end—i.e., the fluid escapes along the upper side of the cylinders, forming an upwash flow. The end effect intensifies such local three-dimensional disturbances, which disrupts the original regular vortex street structure in the wake, triggers its distortion and fragmentation, and further induces high-velocity flow bands and asymmetrically distributed shear layers.

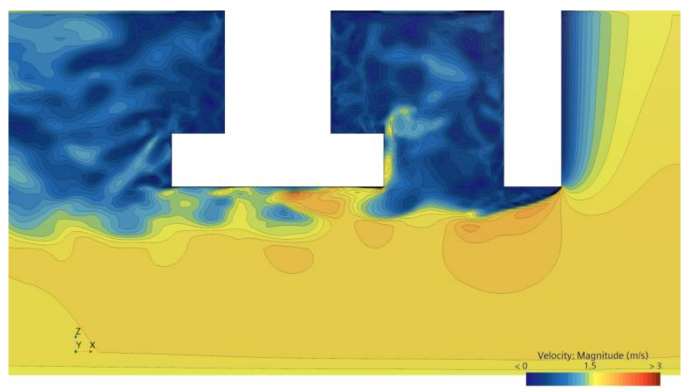

Figure. 8 Velocity magnitude distribution on the x-z cross-section of the downstream cylinder

Figure 8 presents the velocity field of the middle cylinder Col 3 and the rear cylinder Col 4 on the x-z cross-section. Velocity deficit zones are formed due to boundary layer separation in the region between Col 3 and the rear cylinder Col 4 as well as in the downstream region of Col 4. The mottled velocity distribution inside the wake reflects the shedding of large-scale vortex structures and turbulent pulsation phenomena. Due to the free-end effect, an extensive local high-velocity zone also appears in the bottom near-wall region.

Vorticity Field Analysis

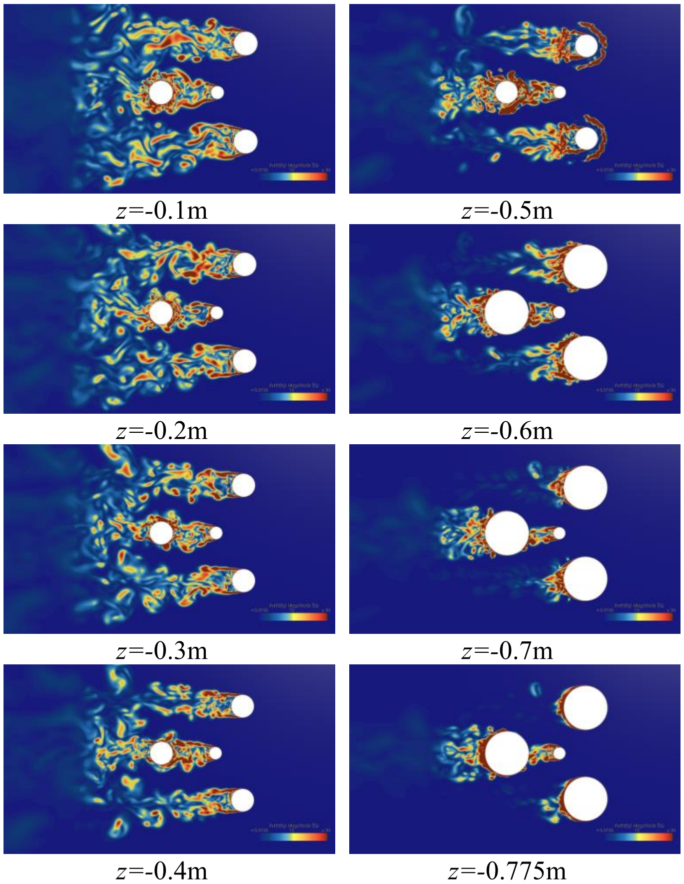

Figure. 9 Vorticity magnitude distribution at different depths

In the shallower depth region (z = -0.1 to -0.3 m), at this point the cross-section is located in the small-diameter section at the upper part of the cylinder. Here, it can be observed that the flow distribution is close to a two-dimensional state. The vorticity field presents a relatively regular Karman vortex street structure, Although there is a weak shear layer lifted in the gap area between the cylinders, there are fewer small-scale turbulent structures, and the flow is mainly dominated by the balance of the main flow inertia and viscosity forces.

Entering the medium-depth water area (z = -0.4 to -0.6 m), at this stage the cross-section crosses the boundary area and transitions from a small-diameter section to a large-diameter section. The complexity of the vorticity field here significantly increases. On one hand, the change in the flow area triggers a local pressure gradient, which leads to the premature separation of the boundary layer and a shift in the phase of vortex shedding; on the other hand, the interference between the wake of the column arrays intensifies, and the vortex shed by the front column is captured or distorted by the rear column during its propagation, resulting in asymmetric stretching, merging, and even fragmentation of the vortex pairs. Dense small-scale high-vorticity spots can be observed in the column gap area, and the instability of the surface shear layer and the intensification of the turbulent cascade process.

In the near-bottom free-end region (z = -0.7 to -0.775 m), at this stage, the cross-section is close to the bottom free end and is significantly influenced by the three-dimensional flow around the free end. The fluid deflects radially outward at the edge of the column base, forming a strong shear layer below the end and in the rear side, and generating a strong, small-scale spiral vortex structure.

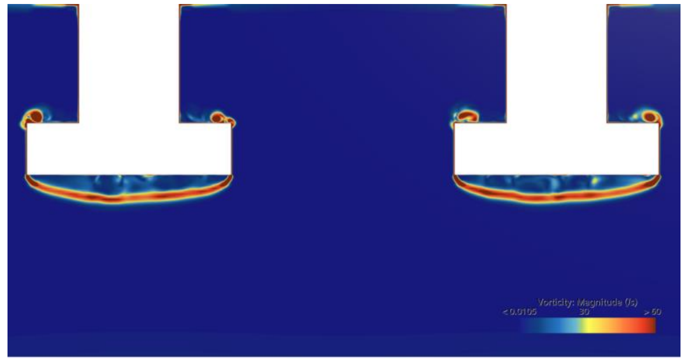

Fig. 10 Vorticity magnitude distribution on the y-z cross-section of the two upstream cylinders.

Figure 10 presents the vorticity field distribution of Col 1 and Col 2 on the y-z cross-section. It can be observed at the interface that the abrupt change in the geometric dimensions of the small and large cylinders induces significant flow separation and vorticity accumulation, forming local high-vorticity regions at the upper and lower edges of the interface. In the near-bottom region, the flow field evolution is dominated by the viscous retardation effect of the bottom surface. The upward transmission of viscous forces forms a continuous high-vorticity shear layer at the cylinder base, and the geometric scale of the large cylinder further enhances the boundary layer separation effect, resulting in a significant increase in the thickness of the high-vorticity band which exhibits a characteristic of developing along the bottom wall in an attached manner.

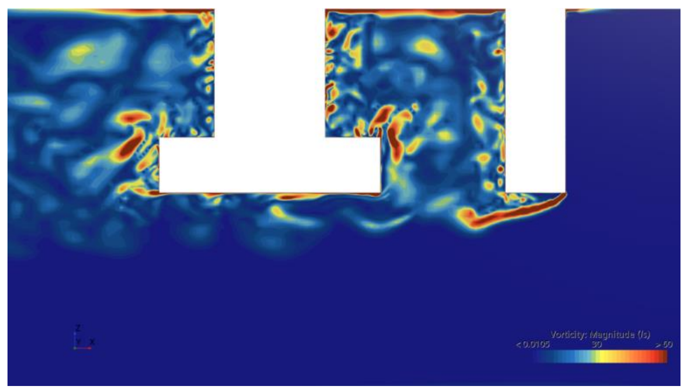

Fig. 11 Vorticity magnitude distribution on the x-z plane of the downstream cylinder.

From the perspective of spatial distribution, in the near free surface region, dominated by the constraint effect of the free surface, the distribution of the flow field vorticity is relatively scattered. The high vorticity areas are distributed in scattered vortex clusters along the side edge of the cylinder, without forming a continuous shear layer. The vertical expansion of the vortex structure by the free surface has significantly inhibited, resulting in a smaller vortex scale and lower vorticity density in the small cylinder section. At the interface, obvious vorticity concentration bands appear at the upper and lower edges of the junction between the middle cylinder Col 3 and the rear cylinder Col 4. The boundary layer of the cylinder at the interface undergoes flow expansion and separation, with a sudden increase in local velocity gradient, inducing the concentration and accumulation of vorticity, forming a high vorticity core area, which becomes the key disturbance source for the evolution of downstream vortex structures. In the near bottom surface region, a continuous and dense high vorticity band forms at the bottom of the cylinder, with the vorticity developing along the bottom wall. The geometric size of the large cylinder further strengthens the boundary layer separation and vortex lifting process, making the near bottom surface region the area with the most concentrated vorticity throughout the cross-section.

From the perspective of cylinder interaction, the wake vortex structures of the downstream middle cylinder Col 3 and rear cylinder Col 4 undergo strong coherent superposition: the wake vortex clusters of the upstream cylinder transfer to the downstream cylinder, and interact with the vortex structure generated by the flow around the rear cylinder. In the gap between the two cylinders, a phenomenon of vorticity stretching and reorganization occurs, with non-uniform strip-like distribution of vorticity in the gap area, and local vorticity showing secondary enhancement. At the same time, the wake interference of multiple cylinders disrupts the vortex symmetry of the single cylinder flow, causing the vortex structure in the xz section to present three-dimensional distortion and asymmetric distribution. The high vorticity area shifts horizontally, while the low vorticity area is fragmentedly distributed.

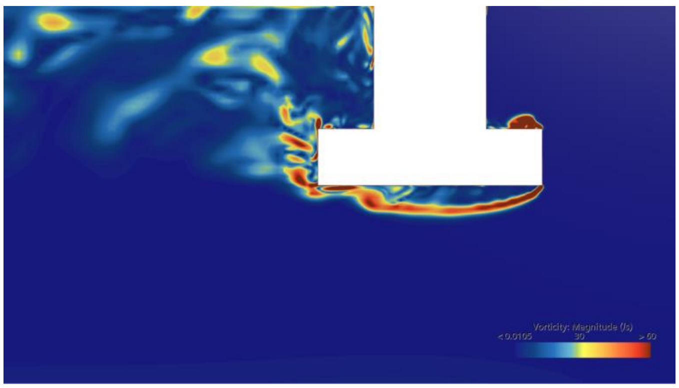

Fig. 12 Vorticity magnitude distribution on the x-z plane of the upstream cylinder

In the interface region, the sudden change in geometric dimensions leads to local flow expansion and intense boundary layer separation, resulting in a significant increase in the flow velocity gradient, which triggers the concentrated generation and accumulation of vorticity, forming a high-intensity vorticity band running across the edge of the interface, becoming the core disturbance source for the evolution of vorticity throughout the cross-section; in the near-bottom surface region, the geometric scale of the large cylinder further intensifies the boundary layer separation process, forming a continuous thick layer of high-vorticity shear layer that develops along the bottom wall, with the vorticity amplitude reaching the secondary peak and being stably distributed in the horizontal direction.

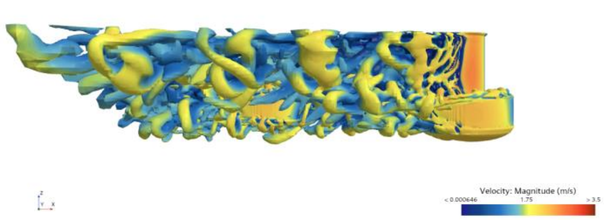

(a)

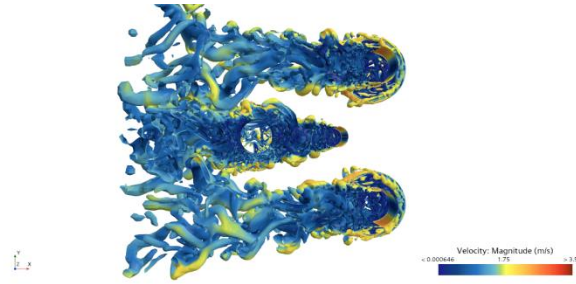

(b)

Fig. 13 Instantaneous Vorticity magnitude Based on Q Criterion：(a) x-z cross-section; (b) x-y cross-section

As can be seen from the Figure 13, the near-wall region generates large-scale coherent vortex structures with high vorticity due to the shear effect of the wall surface, and these vortices periodically fall off due to flow separation. As the flow progresses downstream, these large-scale vortices are stretched and distorted under the action of convection and shear, gradually breaking down into small-scale vortex structures, demonstrating the cascade process of turbulent energy transferring from large scales to small scales. In terms of spatial distribution, the near-wall region has high vorticity intensity and a large spatial scale due to the shear effect of the wall surface. As the vortex structure extends downstream along the flow direction, it gradually spreads, indicating that the vorticity intensity decreases with the development of the flow, and the spatial scale also continuously decreases. At the bottom of the cylinder, the swirling vortex generated at the free end detaches from the end and moves along an upward diagonal trajectory. To a certain extent, it inhibits the development of the counterclockwise flow direction of the Karman vortex street, thereby interfering with its propagation and evolution trend.

CONCLUSIONS

In this study, the STAR-CCM+ software is employed to conduct numerical simulations of the OC4 floating wind turbine platform. The SST-DES turbulence model is adopted, and the coupling mechanism of the cylinder dimension, free end and inter-cylinder interference is systematically investigated. The main conclusions are as follows:

In the multi-column layout, it can be observed that the flow field response is dependent on the position, and the position of the components is the decisive factor for the flow field response. The position of the middle column Col 3 is located at the intersection of the wake zones of Col 1 and Col 2 upstream and is subject to a strong wake shielding effect, resulting in a relatively stable resistance; Col 4 located downstream is affected by the superposition of multiple columns' wakes and the coupling of vortex shedding and detachment, and the fluctuation amplitude of the resistance coefficient is large, thus being the most sensitive component position in the flow field response; while the upstream columns Col 1 and Col 2 are in the direct impact area of the flow field, the flow field coupling effect is weak, and they are in a relatively stable flow-around state.

From the perspective of the stratification of the velocity field and the characteristics of the interference, the flow field as a whole presents a stratified distribution feature of the low-speed zone near the wall, the high-speed zone between the columns, and the low-speed vortex zone in the wake. At the column gap, the velocity gradient is significant, and this area is the core part of the shear flow effect; while downstream of the middle column Col 3, a wake reflux zone is formed, where the flow velocity significantly decreases; the rear column Col 4 is affected by the upstream wake coupling, and the overall flow velocity in the wake zone is lower than the incoming flow, and the fluctuation of the flow velocity and the cycle of vortex shedding and detachment show a high degree of correlation.

In terms of the evolution of the vorticity field, it can be found that with the change of depth, the column flow-around also presents a clear three-dimensional flow evolution law. The flow in the shallow water area is relatively stable, with a regular and orderly vortex structure; in the middle transition section, due to the influence of the pressure gradient and wake interference, the vortex structure is distorted and fragmented, and the turbulent structure is significantly enhanced; in the near-bottom end area, a strong shear layer and spiral vortex structure are formed under the action of three-dimensional flow-around. The overall flow is dominated by the diameter size variation and the bottom end effect.

The upstream column shielding effect affects the energy distribution of the flow field, and the wake vortex decoupling regulates the flow field response of downstream components; the middle column Col 3 assumes the core regulating role of the flow field, the upstream columns Col 1 and Col 2 maintain the symmetry of the flow field, and the position of the downstream column Col 4 is the most sensitive to the wake vortex and resistance fluctuations. The wake superposition and vortex interference between multiple columns jointly shape the velocity stratification, vorticity evolution, and time-varying characteristics of the flow field.

ACKNOWLEDGEMENTS

This work was supported by the National Key Research and Development Program of China (2025YFF0519800), to which the authors are most grateful.

REFERENCES

Chen, S.T., Zhao, W.W., Wan, D.C., and Gao, Y.Y. (2022). "Numerical simulation of flows around a finite-length cylinder with free surface", *Chinese Journal of Ship Research*, 17(1), 91–98.

Gong, Z.J., Yang, J., Wu, W.F., and Li, B.W. (2015). "Simulation of flow patterns and force characteristics of low Reynolds flow past four cylinders using lattice Boltzmann method", *Chinese Journal of Applied Mechanics*, 32(1), 52–56.

Kitagawa, T., and Ohta, H. (2008). Numerical investigation on flow around circular cylinders in tandem arrangement at a subcritical Reynolds number. *Journal of Fluids and Structures*, 24(5), 680-699.

Liu, C. H., and Chen, J. M. (2002). Observations of hysteresis in flow around two square cylinders in a tandem arrangement. *Journal of Wind Engineering and Industrial Aerodynamics*, 90(9), 1019-1050.

Liu, W.M., Gu, J.Y., and Lu, Y.X. (2012). “Numerical simulation of flow around four cylinders in array,” *Journal of Jiangsu University of Science and Technology (Natural Science Edition)*, 26(6), 534–540.

Spalart, P. R., Jou, W. H., Strelets, M., and Allmaras, S. R. (1997). “Comments on the feasibility of LES for wings, and on a hybrid RANS/LES approach,” *in Advances in DNS/LES, eds. C. Liu, Z. Liu (Greyden Press, Columbus, OH)*, 137–147.

Wang, X.C., Gui, H.B., and Liu, Y. (2018). Numerical simulation of three-dimensional flow around a finite-length circular cylinder. *Chinese Journal of Ship Research*, 13(2), 27-34.

Zdravkovich, M. M. (1987). The effects of interference between circular cylinders in cross flow. *Journal of fluids and structures*, 1(2), 239-261.

Zhao, W., and Wan, D. (2016). Numerical study of 3D flow past a circular cylinder at subcritical Reynolds number using SST-DES and SST-URANS.